

## RESEARCH ARTICLE

10.1029/2017JD028170

## Key Points:

- Model-independent analyses of radio occultation, RO, are developed to constrain lapse rates and stability inside clouds
- RO observes how precipitation changes layerwise the lapse rates that define stability to convection in ways missed by weather analyses
- Top of boundary layer inversions leading to refractivity gradients is sharper in nonprecipitating than precipitating scenes

## Correspondence to:

M. de la Torre Juárez and R. Padullés,  
mtj@jpl.caltech.edu;  
ramon.padulles.rullo@jpl.caltech.edu

## Citation:

de la Torre Juárez, M., Padullés, R., Turk, F. J., & Cardellach, E. (2018). Signatures of heavy precipitation on the thermodynamics of clouds seen from satellite: Changes observed in temperature lapse rates and missed by weather analyses. *Journal of Geophysical Research: Atmospheres*, 123, 13,033–13,045. <https://doi.org/10.1029/2017JD028170>




Received 6 JAN 2018

Accepted 28 OCT 2018

Accepted article online 31 OCT 2018

Published online 3 DEC 2018

## Signatures of Heavy Precipitation on the Thermodynamics of Clouds Seen From Satellite: Changes Observed in Temperature Lapse Rates and Missed by Weather Analyses

Manuel de la Torre Juárez<sup>1</sup> , Ramon Padullés<sup>1,2</sup>, F. Joseph Turk<sup>1</sup> , and Estel Cardellach<sup>2</sup> 
<sup>1</sup> Jet Propulsion Laboratory, California Institute of Technology, Pasadena, CA, USA, <sup>2</sup> Institute of Space Sciences ICE, CSIC, IEEC, Barcelona, Spain

**Abstract** Analyses of the thermodynamics of precipitating clouds are mostly based on localized in situ campaigns or, more globally, weather analyses and reanalyses. This work presents a comparison of weather analyses to satellite observations and a radiometeorological method that shows how precipitating layers inside clouds coincide with weather analyses underestimates of the amount of water vapor. The thermodynamic information from inside precipitating clouds is extracted using observed radio occultation (RO) refractivity profiles without requiring weather analysis input, thus reducing analysis-induced biases. The radiometeorological method is described by first identifying the differences between adiabatically dry, mixing-ratio conserving, and saturated pseudoadiabatic refractivity profiles. These reference profiles are then compared to observed RO refractivity profiles within precipitating and nonprecipitating clouds to infer changes in their height-dependent thermodynamic states and in stability to convection. Precipitation is found to start below layers close to pseudoadiabatic and precipitation layers coincide with changes into conditional stability against convection. A statistical comparison between observed profiles and the gradients predicted for a saturated pseudoadiabatic profile is made and finds that on the global average, precipitation separates clouds from the Clausius-Clapeyron law and profiles are close to a saturated pseudoadiabatic. The results (a) help constrain the physical processes associated to precipitation inside clouds and (b) validate the potential of graphical RO techniques to analyze observations without ancillary temperature data from weather analyses.

**Plain Language Summary** Predicting how precipitation responds to changes in atmospheric thermal profiles remains a challenge identified by the Intergovernmental Panel on Climate Change. Solving this challenge requires comparing models with the observed thermodynamics of precipitating clouds. Only radio occultation (RO) can constraint globally the thermodynamics inside clouds with high vertical resolution. Infrared and microwave can measure the thermodynamics outside and only partially clouds, and radar instruments that measure inside clouds do not provide thermodynamic information. This paper develops a method to use RO for distinguishing the thermodynamics inside precipitating versus nonprecipitating clouds. The identification of rain is made using coincidences of RO soundings with Tropical Rainfall Measuring Mission and CloudSat observations. Using the method, we show that globally, (1) the European Center for Medium-Range Weather Forecast ERA Interim reanalysis and the Global Forecast System weather analysis have a global bias in precipitating clouds caused by misrepresentation of the thermodynamics inside clouds; (2) the nature of the bias is associated to a misrepresentation of the lapse rates by the analyses; (3) there are changes in stability to moist convection associated to the height where precipitation originates, and (4) the transition from midtropospheric lapse rates to boundary layer shows more frequent sharp inversions in nonprecipitating than in precipitating scenes.

## 1. Introduction

This manuscript introduces a radiometeorological approach that enables model-independent analyses of vertical temperature gradients, or lapse rates when using the opposite sign, in the atmosphere and the stability against convection inside clouds. Analyses are applied separately into precipitating and nonprecipitating

scenes to find that precipitation changes the observed stability to moist convection layerwise in ways missed by weather analyses and reanalyses.

Modeling precipitation remains an important challenge identified in the fifth Intergovernmental Panel on Climate Change Assessment Report (AR5) as a key uncertainty in the understanding of the climate system and the ability to project changes in its response to anthropogenic influences (Intergovernmental Panel on Climate Change, 2014, and references therein). Proper modeling of precipitation would help many areas that need the prediction of heat waves (e.g., Vautard et al., 2013), extreme precipitation, and the influence of the precipitation cycle on climate feedback processes (Intergovernmental Panel on Climate Change, 2014). Understanding the relation between lapse rates, or the stability to convection, itself linked to the likelihood of heavy precipitation, the vertical water vapor distribution, clouds precipitation, and climate variability, would increase our ability to constrain the vertical distribution of moisture, the altitudes at which clouds form, their life cycle, and hence the Earth albedo at the top of the atmosphere. The cloud life cycle is key to the cloud feedback on climate, a key uncertainty in understanding the drivers of the atmosphere's energy budget (Intergovernmental Panel on Climate Change, 2014, and references therein). Recent investigations have noted the relationship between total column water vapor and a sharp pickup in precipitation associated with the onset of conditional instability (Emanuel et al., 1994), leading to deep convection (e.g., Bretherton et al., 2004). Further studies have proposed that precipitation in clouds may be modulating the hydrological and cloud cycles to cause negative cloud feedbacks (Mauritsen & Stevens, 2015).

Climate and weather forecasting models suffer severe biases because of their inability to represent the dynamics and microphysics of clouds and precipitation adequately (e.g., Intergovernmental Panel on Climate Change, 2014; Padullés et al., 2018; Phillips et al., 2004; Rodwell & Palmer, 2007, and references therein). The limited skill of current weather analyses to accurately capture the conditions for precipitation compared to observations is illustrated in Figure 1, discussed in section 2 of this work, and in Padullés et al. (2018). The discrepancies have been attributed to factors from the influence of numerical resolution (e.g., Kotlarski et al., 2014), the need of analyses to improve convection parameterizations, or to the need of capturing the wide range of microphysical properties that can be found in cloud particles. The challenge is to model and predict the large-scale effects of the interactions between tiny cloud particles, turbulence, and large-scale atmospheric flows associated to precipitation. Insight into this large-scale interaction on a planetary scale is provided by identifying observations that enable a better understanding of the thermodynamics and convective states associated to precipitation in clouds and that can validate weather analyses.

Observations exist that complement and validate weather models results. Dedicated field campaigns with radiosonde and airborne measurements provide detailed information on specific events but have limited geographical and temporal coverage. On a global scale that covers the whole planet and the different seasons, satellite optically visible, infrared, and microwave instruments provide additional information albeit at lower spatial resolution. However, infrared instruments that provide thermodynamic information of the atmosphere and even some cloud particle properties (e.g., Platnick et al., 2003) cannot measure temperature and water vapor distributions inside thick clouds (Wulfmeyer et al., 2015, for a review). Radar and laser instruments that can track precipitation and particle properties inside precipitating clouds do not measure the coincident pressure, moisture, and temperature. Microwave instruments such as the Advanced Microwave Scanning Radiometer-Earth Observing System provide precipitation rates as total integral magnitudes and vertical moisture profiles at vertical resolution coarser than a kilometer. This work uses radio occultation (RO) of the Global Navigation Satellite System (GNSS) obtained from the Constellation Observing System for Meteorology, Ionosphere and Climate (COSMIC; Anthes et al., 2008). RO measures refractivity inside clouds, a combination of atmospheric pressure, temperature, and water vapor information (Kursinski et al., 1997; Thayer, 1974). RO profiles are used in this work with coincident radar observations to characterize the lapse rate thermodynamics of precipitating clouds over oceans and land. Analyses of the thermodynamics of clouds have been performed before using standard RO retrievals (e.g., Biondi et al., 2013; Xian & Fu, 2015; Yang & Zou, 2017) and those required ancillary temperature profiles from a weather analysis (e.g., Anthes et al., 2008; Baerkgard et al., 2014; Hocke, 1997; Kursinski et al., 1997, and references therein for details). This work presents a novel method to do the same without requiring ancillary data and the results.

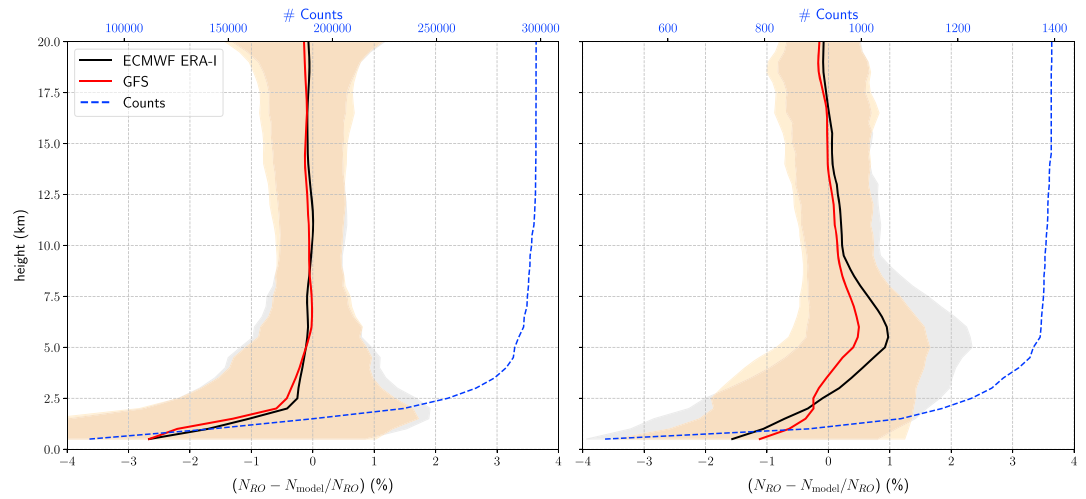


**Figure 1.** Comparison between Constellation Observing System for Meteorology, Ionosphere and Climate refractivity profiles and weather models in the presence of precipitation versus absence of precipitation according to the Integrated Multi-Satellite Retrievals for the Global Precipitation Mission data product. Left shows the mean (line) and standard deviation (shaded area) differences between the measured and the analysis and reanalysis  $N$  without rain. Right shows the same analysis for cases with heavy rain. The RO profiles compare to an analysis and a reanalysis (red, GFS, and black, ECMWF-ERA interim reanalysis). Heavy rain is defined as the top 5% of cases with rain, sorted by maximum reflectivity in the surroundings of the RO. The brown-shaded region shows the standard deviation for the differences from RO to GFS, while the gray shading shows the standard deviation to ECMWF-ERA. ECMWF-ERA = European Center for Medium-Range Weather Forecast; GFS = Global Forecast System; RO = radio occultation.

## 2. Data and Approach

The data used are observed vertical profiles of GNSS RO refractivity from COSMIC (Anthes et al., 2008) compared to the refractivity profiles predicted for different thermodynamic conditions. The profiles were separated into precipitating and nonprecipitating scenes based on the existence of coincident precipitation radar profiles from the Tropical Rainfall Measuring Mission (TRMM; Kummerow et al., 1998), a joint U.S.-Japan satellite mission to monitor tropical and subtropical precipitation that provided data until 2015. The orbital 3D 2B31 TRMM data products were obtained from the data server at NASA Goddard (version 07 on <ftp://trmmopen.gsfc.nasa.gov>). The CloudSat W-band cloud profiling radar (Stephens et al., 2002) 2B-GEOPROF data product was also used to identify small particles associated to clouds. Coincidences between TRMM, CloudSat profiles, and COSMIC were sought from 1 June 2006 to 31 December 2016 (Cardellach et al., 2017). The criterion was to look for locations within the swath area of the TRMM satellite radar, or within 50 km of a CloudSat scan. The radar measurements had to be within 15 min of the RO event. With these criteria, there were 16,881 RO profiles near a TRMM radar swath, and 5,125 collocations with CloudSat. In this analysis we did a height-dependent comparison.

Refractivity,  $N(z)$ , is the RO observable, a combination of pressure,  $p$ ; temperature,  $T$ ; and water vapor pressure,  $e$  (e.g., Thayer, 1974). Liquid and ice phase water contributions can be neglected because of being comparable or less than the 0.5% estimated error from the coefficients in the formula for total refractivity (e.g., Bean & Dutton, 1966; Solheim et al., 1999; Yang & Zou, 2017).  $N$  is thus not very sensitive to changes in the phase of atmospheric water. From the RO profiles observed  $N$  one can calculate or at least constrain pressure, temperature, and water vapor content. Using  $e = p * r / (e + r)$  with  $r$  being water vapor mixing ratio,  $p$  pressure,  $e$  water vapor pressure,  $T$  temperature,  $z$  height, and  $\epsilon = R_d/R_v = 0.622$  the ratio of the gas constant for dry versus moist air:

$$N(z) = k_1 \frac{p(z)}{T(z)} \left[ 1 + k_2 \frac{r(z)}{\epsilon + r(z)} \left( 1 + \frac{k_3}{T(z)} \right) \right], \quad (1)$$

with  $k_1 = 77.6$  K/hPa,  $k_2 = -0.0927835$ , and  $k_3 = -51930.56$  K.

While some geometric information like where is the top of clouds and the thermal inversion above them has been inferred from refractivity without model input (e.g., Biondi et al., 2012; Peng et al., 2006), analyses of RO profiles thermodynamics inside clouds have been using water vapor profiles that are retrieved from RO by

incorporating input from the weather analysis. In a dry atmosphere, where  $r = 0$ , given an initial height,  $z_0$ , typically chosen at heights above the clouds, and given a pair of values for  $(N(z_0), p(z_0))$  one can use equation (1) to get pressure and temperature from the observed RO refractivity at lower levels  $z < z_0$  down to the surface level  $z_s$  by applying hydrostatic balance as a constraint (e.g., Hocke, 1997; Kursinski et al., 1997). However, when  $r > 0$  one has 3 unknowns,  $(p, T, r)$ , to retrieve from one observable,  $N$ , and only one equation and a constraint, hydrostatic balance. With less equations than variables the problem is undetermined. RO retrievals typically use weather models temperatures to separate water vapor pressure in the observed refractivity (e.g., Anthes et al., 2008; Baerkgard et al., 2014; Kursinski et al., 1997, and references therein) by assuming that the models have the right temperature and using the models temperature in equation (1) to calculate  $r$  from the observed  $N$ . Hence, analyses of RO-based water vapor, temperatures, and lapse rates inside clouds depend on the quality of temperature and refractivity profiles in the analyses used in the standard RO retrievals. Figure 1 compares refractivities from COSMIC RO soundings within clouds to the public 2.5° resolution version of the weather reanalysis from the European Center for Medium-Range Weather Forecast (ECMWF-ERA) Interim reanalysis and the Global Forecast System (GFS) from the National Centers for Environmental Prediction with and without precipitation averaged vertically in bins of 0.5 km. Both are used in the RO retrievals and available from the COSMIC web archive data server, COSMIC CDAAC, after interpolating to the time and location of the RO tangent point. Because RO has different vertical height levels for each given location, the number of vertical measurements inside each 0.5 km vertical bin differs, and coincidences can change as a function of height. Additionally, the count of profile comparisons drops off closer to the surface, reflecting the fact that RO receivers can lose track of the signals due to topography, multipath, and superrefractive layers caused by sharp water vapor and temperature transitions between the planetary boundary layer and the free troposphere (e.g., Bean & Dutton, 1966; Kursinski et al., 1997). Sharp boundary layer transitions cause a decrease in the count of coincidences in Figure 1 for the lowest 2 km of the atmosphere. At heights below 5 km, where precipitation is more likely to occur, the observed refractivity is larger than the weather model especially at low latitudes even though ECMWF and GFS incorporate RO data. Studies (e.g., Yang & Zou, 2017) show that it often happens for clouds, and Figure 1 shows that it is in the presence of precipitation. A more detailed comparison finds similar results when using the ECMWF high-resolution reanalyses globally and regionally, and this difference has been traced back to errors in the weather analyses (Padullés et al., 2018, for more details). Refractivity errors expected in RO have been quantified to lie between 0.2% at 8-km height, 0.6% at 4 km, and increase up to 1% at the surface after considering receiver tracking errors and multipath. Errors of 1–2% have been achieved even under superrefractive layers (Wang et al., 2017) confirming these predictions, although the method is not yet in existing operational RO retrieval systems. The quantitative discussion here addresses, therefore, mostly observations in the free troposphere, above the top of the boundary layer. The largest contribution stems from the possible influence of horizontal frontal structures along the RO ray path (estimated for a ray path crossing a strong front in Figure 10 of Kursinski et al., 1997). The contribution to refractivity by liquid water and ice in typical atmospheric conditions add up to a negligible fraction of 1% (e.g., Kursinski et al., 2000; Padullés et al., 2018; Yang & Zou, 2017). These errors are lower than the peak difference measured between observed and modeled refractivities in Figure 1 at 5 km. An additional error source, at the lowest altitudes of RO profiles, emerges from the transition from a positive to a negative refractivity bias occurring from the top of the boundary layer down, usually from ~3 km down. Notice, however, that the precipitating scenes show a smaller negative bias below 3 km than the nonprecipitating, which would be expected if there are less superrefractive layers, meaning smoother transitions at the top of the boundary layer. The discrepancy observed above 3 km has two consequences. The first is that model parameterizations of the precipitation needs improvement in near equatorial regions. Second, given that the observed RO refractivity is higher than the weather model, the reliability of operational RO retrievals using the weather analyses temperatures is lower. Our ability to analyze the moist thermodynamics of precipitation from either weather model, as done in most of the available literature, or standard RO retrievals (e.g., Biondi et al., 2013; Biondi et al., 2012; Bonafoni & Biondi, 2016; Vergados et al., 2014) is lower and therefore one benefits from model-independent validation. Those situations where weather models and RO differ are where RO soundings are most useful to identify and correct errors in the weather prediction models. A model-independent analysis of cloud thermodynamics appears thus beneficial to extract information from these profiles and is a motivation for this work.

### 3. Isothermal, Adiabatic, and Pseudoadiabatic Refractivity Profiles

Atmospheric thermodynamic diagrams are used in radiosonde meteorology to plot the observed temperature as a function of pressure overlaid with different lines that correspond to the  $T(p)$  that would occur in different thermodynamic processes (e.g., Bezold, 1888; Dutton, 1976; Hertz, 1884). Examples are isotherms; lines of constant mixing ratio; and lines where temperature changes conserving entropy or where pressure, temperature, and specific humidity follow saturated pseudoadiabatic ascent. Similarly, one could apply to a RO profile each thermodynamic constraint to infer refractivity gradients and calculate the profiles downwards from any upper boundary condition  $N(z_0)$ ,  $p(z_0)$  at a height  $z_0$  high enough for moisture to be very low and negligible.

#### 3.1. Isothermal Refractivity Profiles

For an isothermal profile,  $T(z) = T(z_0)$ , hydrostatic balance leads to  $p(z) = p(z_0)e^{-g(z-z_0)/[RT(z_0)]}$  with  $g$  gravity and  $R$  the atmospheric gas constant. Note that in the presence of moisture,  $R$  would include a water vapor contribution and  $T$  would be the virtual temperature, but we are ignoring this correction for now since we are focusing on a conceptual discussion that leads to an analytical solution. The correction will be included in the subsequent discussions with comparisons to the data. Applied to (1) an isothermal atmosphere in hydrostatic balance yields

$$N(z) = k_1 \frac{p(z_0)}{T(z_0)} e^{-\frac{g(z-z_0)}{RT(z_0)}} \left[ 1 + \frac{k_2 r(z)}{\epsilon + r(z)} \left( 1 + \frac{k_3}{T(z_0)} \right) \right]. \quad (2)$$

Hence, for an  $(N(z_0), p(z_0))$  pair, hydrostatic balance and the isothermal condition  $T(z) = T(z_0)$ , refractivity will depend only on the moist thermodynamics of  $r(z)$  at each height  $z$ . For an isothermal profile that conserves water vapor mixing ratio with height,  $r_0 = r(z) = r(z_0)$ , so that  $N(z) = N(z_0) \exp[-g(z-z_0)/RT(z_0)]$ . These exponential models of refractivity have been used often in the literature (e.g., Bean & Dutton, 1966).

#### 3.2. Adiabatic Dry and Moist-Conserving Refractivity Profiles

Moisture conserving isothermal profiles as described above are unlikely in the atmosphere but serve as a good illustration before extending this approach to thermodynamic conditions more realistic that require numerical solutions. If a RO sampled a moist adiabatic atmosphere with well-mixed water without sources or sinks of water vapor, mixing ratios would remain constant,  $r(z) = r_0$ . Air parcels undergoing adiabatic ascent conserve the potential temperature,  $\Theta$ , (Bezold, 1888) whose logarithm is proportional to entropy, or the heat exchange per unit temperature, and temperature depends linearly on height:  $T(z) = T(z_0) - \Gamma_a(z - z_0)$ . For a dry atmosphere with  $r_0 = 0$ , the adiabatic lapse rate is  $\Gamma_a = g/C_p$  with  $C_p$  the heat capacity at constant pressure. Hydrostatic balance then leads on this linear temperature profile to  $p(z)/p(z_0) = [T(z)/T(z_0)]^{-g/RT_a}$  (e.g. Dutton, 1976) and

$$\begin{aligned} N_{dry}(z) &= k_1 \frac{p(z)}{T(z)} \left[ 1 + \frac{k_2 r(z)}{\epsilon + r(z)} \left( 1 + \frac{k_3}{T(z_0) - \Gamma_a(z - z_0)} \right) \right] = \\ &= k_1 \frac{p(z_0)}{T(z_0)} \left[ \frac{T(z)}{T(z_0)} \right]^{-\frac{g-RT_a}{RT_a}} \left[ 1 + \frac{k_2 r(z)}{\epsilon + r(z)} \left( 1 + \frac{k_3}{T(z)} \right) \right]. \end{aligned} \quad (3)$$

For an initial  $N(z_0)$ ,  $p(z_0)$  condition at the top, hydrostatic balance, entropy conservation, and conserved mixing ratio lead to a family of refractivity profiles, one profile for each value of constant  $r_0$  that can be generated using the original  $T(z_0)$  also if it corresponds to a different  $N(z_0)$ . This refractivity with constant moist potential temperature is related to what has been termed *potential refractivity modulus*,  $\Phi$ , in the literature (e.g., Bean & Dutton, 1966; Lukes, 1944, in their Figure 5.17, use A-units that are somewhat related) to perform graphical analyses of refractivity in the past. Potential refractivity for a dry atmosphere with  $r = 0$  is seen in Figure 2 left panel where a dry isentropic refractivity profile is next to an observed occultation profile and the ECMWF-ERA Interim model interpolated to the location and time of the RO. The initial value of  $N(z_0)$  and  $p(z_0)$  at the cold point tropopause has been propagated down isentropically and so is the potential refractivity  $N_{dry}(z)$  profile (red) for a dry atmosphere. At lower altitudes, where water vapor becomes significant, moist potential refractivity has to be considered, and different initial values of  $r(z_0)$  between zero and 12% at  $z_0$  and  $p(z_0)$  have been used with different initial values of  $N_{dry}(z_0)$  and the formula (3) to create a family of  $r$  conserving potential refractivity lines shown as dashed red with annotation lines on the right panel of Figure 2. In the following, we refer to dry adiabatic profiles when  $r = 0$  and moist-conserving adiabats when the atmosphere is moist and considered constant independently of its being saturated or nonsaturated  $r(z) = r(z_0)$  (e.g., following formula 4.2.11 Emanuel, 1994). These profiles represent reversible thermodynamic processes.



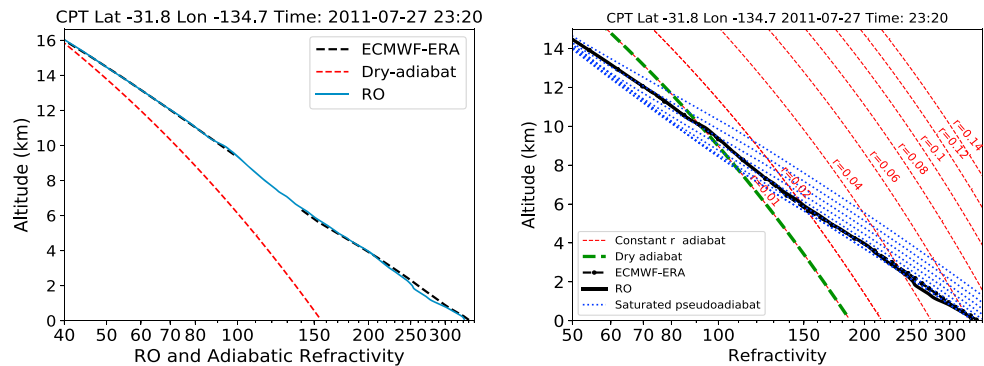


**Figure 2.** Left: observed RO profile on 27 July 2011 (solid line) compared to the public version of the ECMWF-ERA Interim reanalysis (black dashed) and the dry isentropic refractivity profile (red dashed line) propagated down from the cold point tropopause; Right: those represented by constant dry and moisture conserving potential temperatures. The solid line is the RO profile, dashed red lines show moisture conserving adiabats for different values of  $r(z)$ . The leftmost dashed green line is the dry adiabat ( $r(z) = 0$ ). It overlaps the red line for the reversible moisture conserving adiabat with  $r(z) = 0.01$ . Blue dots mark saturated pseudoadiabatic profiles. The observation coincided with rain, and the figure shows higher gradients (separating from the moist saturated pseudoadiabat) at altitudes below 10 km and lower gradients, close to moist pseudoadiabats above 10 km. ECMWF-ERA = European Center for Medium-Range Weather Forecast; RO = radio occultation.

### 3.3. Moist Pseudoadiabatic Refractivity Profiles

On a further step, atmospheric processes with a variable lapse rate can be also addressed by discretizing the atmosphere into multiple thin layers each with a locally constant temperature lapse rate between two heights. Equation (3) is then solved between each two heights by replacing  $\Gamma_a$  by a  $\Gamma$  that is constant only within each layer and updated after using  $\Gamma$  to predict the temperature at the layer below. An important application example is the moist saturated pseudoadiabat,  $\Gamma_m$  (e.g., Emanuel, 1994, formula 4.7.3) treated as constant within thin layers but changing from one to the next one below. Starting with an initial condition  $p(z_0)$ , at an arbitrary but high altitude  $z_0$  where moist refractivity is negligible, one can postulate a family of temperature values  $T(z_0)$ , and their saturation mixing ratios  $r_s(z_0)$  are used to numerically generate a family of saturated refractivity profiles, each stemming from an initial  $\Gamma_m[T(z_0)]$ , which is then used to predict  $T(z_1)$  at the slightly lower height  $z_1 = z_0 - \Delta z$ , infer its saturation water vapor pressure  $e_s(z_1)$ , use then hydrostatic balance to infer  $p(z_1)$  and  $r_s(z_1)$ , and from there  $N(z_1)$ . Proceeding layer by layer leads to the family of moist saturated pseudoadiabatic  $N_{pseud}(z)$  profiles marked as dots in Figure 2. An alternative approach also explored numerically was to draw the lines of refractivity profiles with constant equivalent potential temperature (e.g., Bezold, 1888; Emanuel, 1994, formula 4.7.9) for each initial combination of  $T(z_0)$  with  $p(z_0)$ . At the discrete vertical resolution used in our simulations both methods end up accumulating a small difference of  $\Delta T \sim 2K - 3K$  at the bottom of the refractivity profiles when initiated from  $z_0 = 14$  km. Using that the uncertainties in lapse rate relate as  $\Delta\Gamma/\Gamma \sim \Delta T/T + \Delta z/z$ , the error is driven by the temperature uncertainties and equivalent to a relative difference of  $\sim 1.2\%$  in lapse rate, which makes both methods virtually equivalent. Dots in Figure 2 marking the pseudoadiabatic saturated atmosphere (constant equivalent potential temperature) show that a saturated pseudoadiabatic atmosphere has a higher vertical refractivity gradient than a moist unsaturated adiabat. Note that while temperature lapse rates are smaller in a saturated than in a dry atmosphere, refractivity being proportional to atmospheric density has a higher lapse rate in a saturated than a dry atmosphere.

Each profile with a different thermodynamic process that starts from a given  $N(z_0), p(z_0), T(z_0)$  exhibits a unique slope. For each observed refractivity we have the three unknowns,  $p$ ,  $T$ , and  $r$ , and one hydrostatic constraint. Given that the hydrostatic constraint is in the derivative, it is a condition on the pressure gradient between two consecutive heights. Thermodynamics add a second constraint that works also on either the vertical gradients of moisture or on temperature. One has now one observation point,  $N$ , and two constraints, which is enough to infer the thermodynamics occurring in three variables inside one layer between two altitude levels. As a consequence, moist thermodynamic processes that can be differentiated in their vertical gradients provide a second constraint needed to uniquely determine the refractivity lapse rate. For instance, a starting  $(N(z_0), p(z_0))$  pair would be crossed by several moist adiabatic curves, each with a different  $(r(z), T(z))$  pair and thus also different slope.

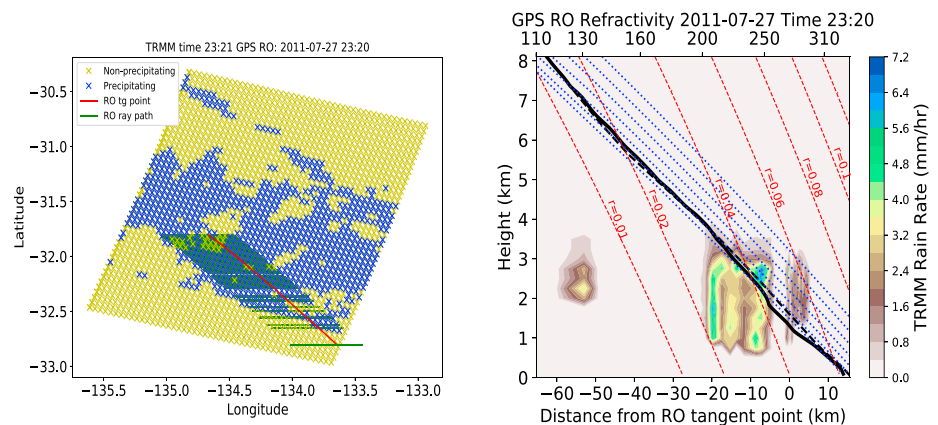


**Figure 3.** Left panel shows the tangent points (red) at all heights of the RO overlaid with a coincident TRMM sounding with precipitating (blue) and nonprecipitating (yellow) pixels. Green lines show the RO raypath direction at each tangent point. Right shows the TRMM precipitation rate in color levels as a function of height along the RO raypath and distance (bottom x-axis labels) to the RO tangent point. Black lines show the refractivity profile, measured by RO (thick solid) and the ECMWF (thick dashed) reanalysis profile, refractivity labels on the top x-axis, compared to the saturated pseudoadiabatic profiles (blue dots) and moist isentrope (thin red dashed) using the approach in Figure 2. ECMWF = European Center for Medium-Range Weather Forecast; RO = radio occultation; TRMM = Tropical Rainfall Measuring Mission.

### 3.4. Thermodynamics Observed in Precipitating Clouds

The method described above is used next to analyze the thermodynamic state of the atmosphere inside clouds in the presence of precipitation without requiring model input. The database of coincident observations between CloudSat and COSMIC RO, and TRMM and COSMIC RO described in section 2 was used. Figure 3 shows the RO raypath from Figures 2 over a coincident precipitating TRMM scene. The right panel shows the rain rates at each latitude-longitude location along the RO rain path as a function of height compared to the coincident RO refractivity profile. The refractivity that would correspond to the publicly available version of the ECMWF-ERA Interim reanalysis at the UCAR-COSMIC CDAAC is also shown as a dashed black line.

Four thermodynamic regimes appear as a function of height in this particular profile. Above the top of the precipitating cells, 6 km, the observed RO refractivity (solid black line) is slightly higher than the weather reanalysis and lower below 6 km. Above precipitation levels, the RO gradient lies between the blue dots marking the pseudoadiabatic and the dashes for the (reversible) moist adiabat. Red dashed lines mark different values of  $r(z_0)$ . Observation and ECMWF-ERA Interim show a similar refractivity at 8 km. At 6 km the ECMWF-ERA Interim reanalysis misses a refractivity structure by overestimating the refractivity lapse rate and approaching a dry adiabat, which suggests a model underestimate in the amount of water vapor. Agreement is restored at about 5 km. Between  $\sim 5$  and 4 km, immediately above the top of the heights where TRMM finds the highest rain rates, the observed (black) and ECMWF-ERA Interim  $N(z)$  follow closely the pseudoadiabatic. Below 4 km, within the precipitation regime, the observed refractivity gradient again separates from the ECMWF-ERA Interim reanalysis and the saturation pseudoadiabatic, crossing the dotted lines, having a steeper slope than saturated moist adiabats do, but remaining between both. This indicates that rain coincides with an observed decrease with altitude in the average RO water vapor mixing ratios suggesting some drying associated with rain in this scene. This layerwise analysis of the observed RO refractivity gradients suggests that the top of precipitation is below layers that, averaged along the RO ray path, follow a pseudoadiabatic and that the loss of water at 4 km dries out the precipitating atmosphere layer below and separates the lapse rate slightly from that of a saturated moist pseudoadiabatic. An effect missed by the model analysis. The observations however do not have the temporal resolution to answer if the drier lapse rate existed at that layer as precondition, during, or as a consequence of precipitation. Below about 1.5 km the vertical refractivity gradient approaches again the saturated pseudoadiabatic and shows no signs of the negative refractivity bias error typical in RO profiles that cross under superrefractive layers.

### 3.5. Stability of Refractivity Profiles

An additional diagnostic is the sign of the difference between the observed refractivity gradient and the refractivity gradient for the different adiabatic  $N_{dry,pseud}$  profiles.

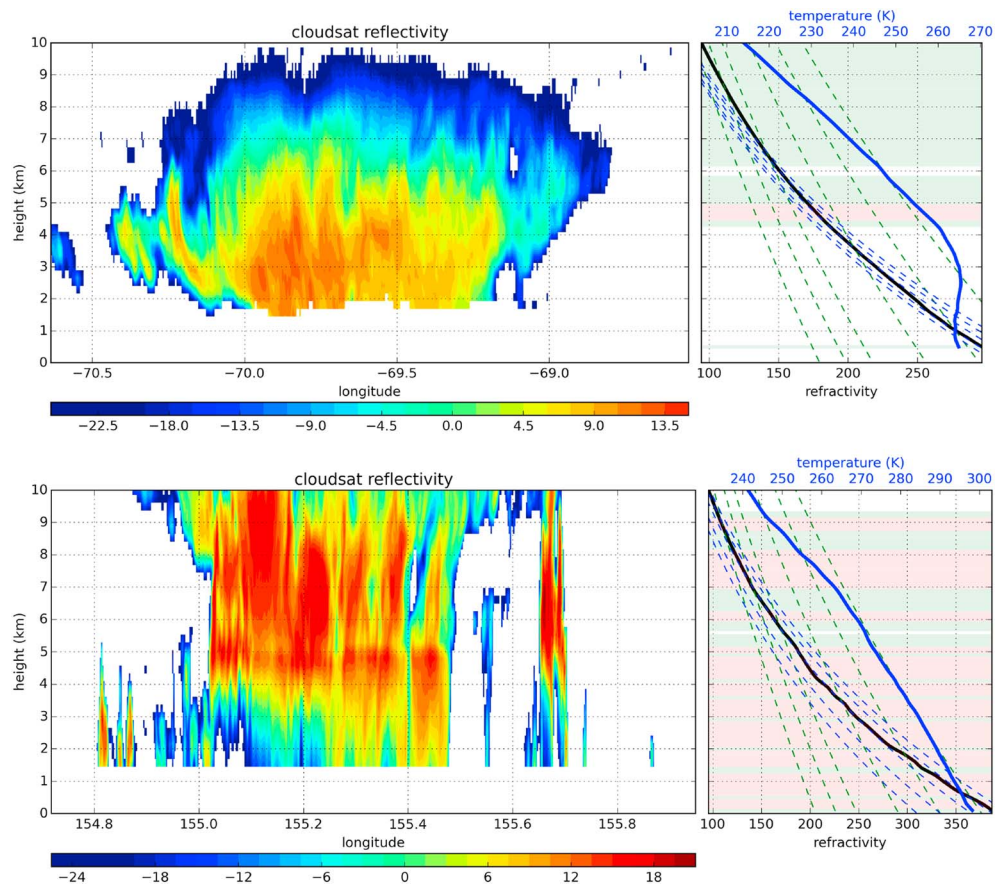


**Figure 4.** Two coincident radio occultation and CloudSat radar profiles. For each occultation, left panels show the CloudSat reflectivity along the radio occultation raypath, the color bar shows reflectivity in units of dBZ. Right panels show the refractivity as a black solid line, temperature from the model in blue, and the stability against moist/dry convection (red/green bands) based on refractivity gradients. Thin dashed lines show refractivity profiles that would correspond to profiles that would be moist-conserving adiabatic in blue and to the saturated pseudoadiabats in dashed black. White horizontal bands signal conditionally stable layers.

- A positive difference between the RO refractivity gradient minus the dry adiabat is stable to dry and moist convection (Bean & Dutton, 1966);
- if the RO refractivity gradient is less than the saturated pseudoadiabat, it is absolutely unstable to dry and saturated moist convection; and
- if the difference is in-between both adiabats, it is conditionally stable: stable to saturated pseudoadiabatic convection if the air is saturated, but the air is unstable if it is dry.

This analysis is equivalent to the standard analysis done with radiosonde data in temperature lapse rates but uses refractivity and overcomes having to know the temperature profile. Figure 4 finds the top of cells with high CloudSat reflectivity associated with the transition from an atmospheric layer stable to moist convection into a layer unstable to moist convection. High CloudSat reflectivity is often associated with precipitation especially when the signal is lost in the lower atmosphere, where intense precipitation is one reason to lose the CloudSat radar frequencies. The first occultation, on top panel, shows a rather homogeneous cell with a narrow range of top heights where precipitation may be occurring. Instability against moist convection (red horizontal lines) is found near the top of the precipitating layers, and, like in Figure 3, the refractivity profile is conditionally unstable (white) below the upper part of the precipitating layer detected by CloudSat and even in areas below, where rain is measured. The second case, bottom panel of Figure 4, includes what seems to be at least two precipitating cells and a more widespread range of heights for the tops of precipitation captured by CloudSat, ranging from above 10 km in one cell to about 7–8 km in a second cell. There is also a wider range of heights where the atmosphere is unstable to moist convection, with changes in stability nearly coinciding



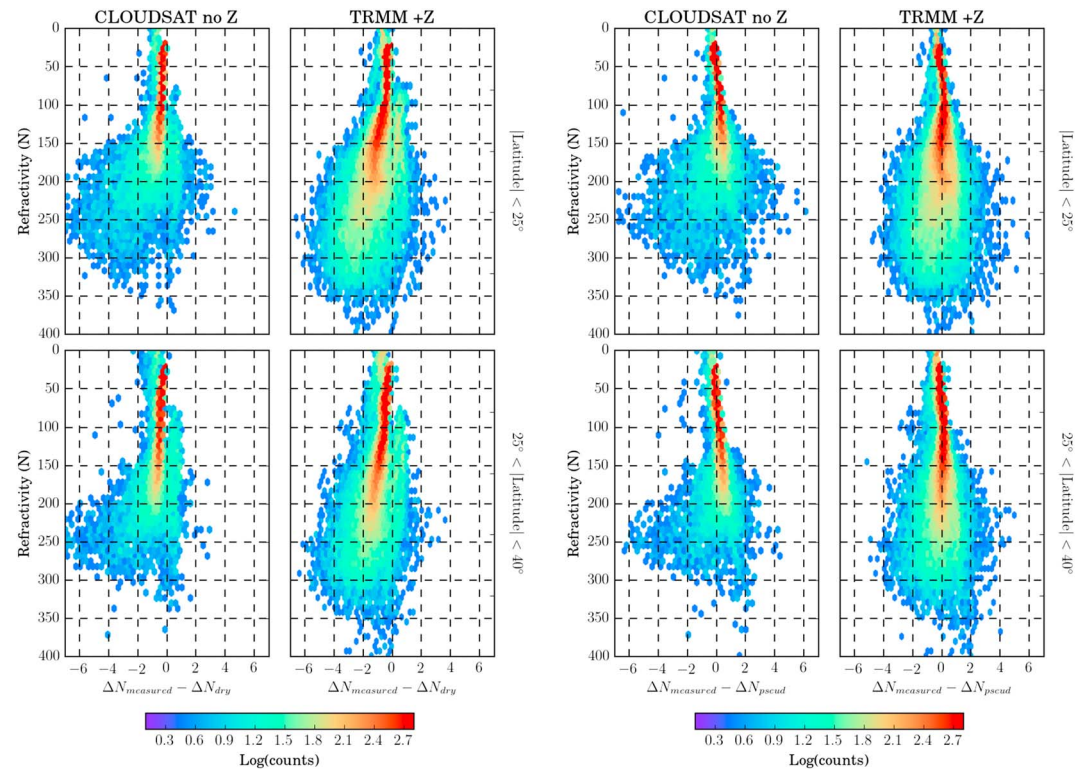


**Figure 5.** Two-dimensional histogram of the percent differences between the observed vertical gradient of radio occultation refractivity and dry adiabat (two leftmost columns) or the saturated pseudoadiabat (two rightmost columns) for a set of  $\sim 1,000$  coincident radio occultation profiles with TRMM and CloudSat. For each comparison, left panels show the differences in clear (reflectivity  $Z \leq -20$  dBZ) versus precipitating (reflectivity  $Z > 30$  dBZ) scenes at latitudes within  $25^\circ$  from the equator (top row) and  $25^\circ$ – $40^\circ$  (bottom row). TRMM = Tropical Rainfall Measuring Mission.

with the range of top heights for precipitation cells. This analysis thus shows that changes in precipitation state from CloudSat relate to changes in the type of stability to convection inferred from RO.

Horizontal inhomogeneities in the rain cells, if estimated to have small influence (Kursinski et al., 1997, 2000), are present in Figure 4 and might account for some of the deviation of the observed RO refractivity lapse rate from the pseudoadiabat. Horizontal inhomogeneities have been argued to play statistically a small role however in RO (e.g., Kursinski et al., 1997; Yang & Zou, 2017) and in the observed dynamics of water vapor columns (Schiro et al., 2016, more recently). One way to minimize the effect of horizontal rain cell inhomogeneities is by increasing the number of profiles observed. If precipitation sources come from the layers with a refractivity profile close to a pseudoadiabat, the effect should be observed in many profiles and, if the correlation between precipitation and pseudoadiabatic gradients were random, it would cancel out for a large number of profiles. The statistics in Figure 5 compare dry and pseudoadiabatic refractivity gradients from about 1,000 observed RO refractivity lapse rates within clear scenes from CloudSat defined as having reflectivity below  $-20$  dBZ, and precipitating clouds from TRMM, defined as those with reflectivity above  $30$  dBZ, separated between the regions of  $25^\circ$ – $40^\circ$  latitude and equatorward of  $25^\circ$  latitude. The comparison uses families of dry adiabats and saturated pseudoadiabats from many initial refractivity values at a given height, say  $z_0 = 20$  km. For each refractivity a  $(p, T)$  surface is created that corresponds to its many possible values of pressures and temperatures. Refractivity is propagated downwards from each point on that surface to generate dry and pseudoadiabatic refractivity profiles in vertical steps of  $0.1$  km. Each lower height has a set of refractivity values that started from a  $(p, T, r)$  value at the top. The vertical gradients and refractivities at each height are saved into a look-up table for the dry adiabat propagated with  $r = 0$ , and for the saturated pseudoadiabat. At each altitude the RO measured refractivity value is matched with the corresponding refractivity in the look-up table and the average vertical gradient from all dry adiabats and moist pseudoadiabats with the same refractivity as observed is compared separately to the observed vertical derivative. Refractivity is the vertical coordinate instead of altitude. The difference in the profiles on the top figure captures that on the global average,

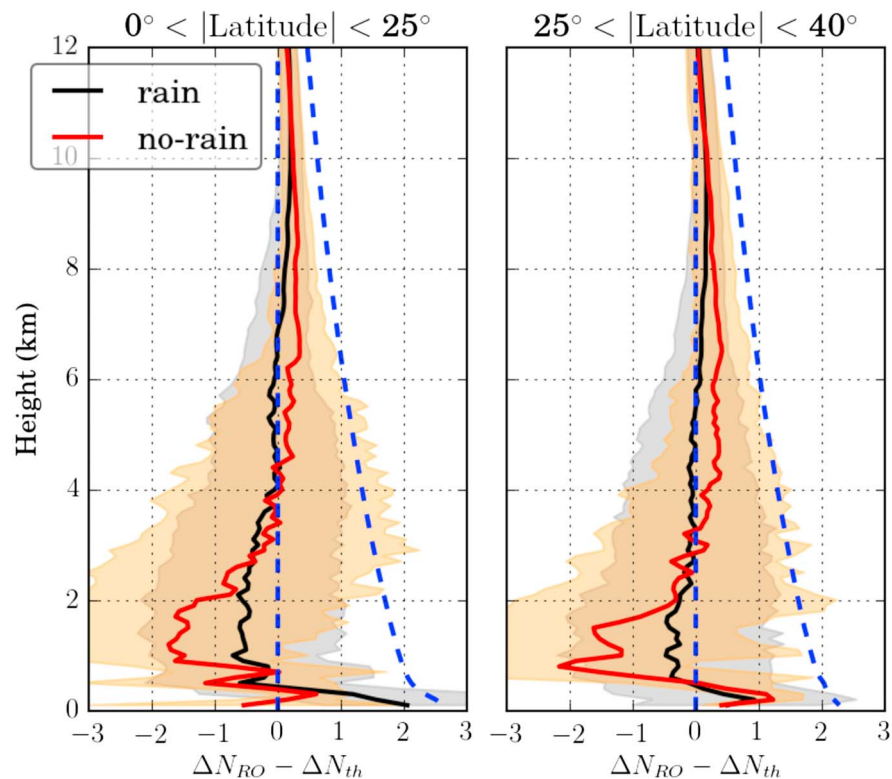


**Figure 6.** Differences between the observed vertical gradient of radio occultation refractivity and the pseudoadiabatic theoretical line,  $N^{\text{th}}$  for a set of  $\sim 1,000$  coincident radio occultation profiles with TRMM and CloudSat. A dry adiabat is shown as the rightmost dashed blue line and the saturated pseudoadiabat is the vertical blue dashed line. Red lines show the average of the differences for clear scenes based on CloudSat reflectivity  $Z \leq -20$  dBZ and black for precipitating clouds ( $Z > 30$  dBZ) within  $25^\circ$  (left panel) and beyond  $25^\circ$  from the equator on the right. The brown-shaded regions show the standard deviation for the differences in the nonprecipitating scenes while the gray region shows the standard deviation during rain.

precipitating clouds have vertical gradients closer to the pseudoadiabat at deep tropical latitudes. In the absence of clouds the 2-D histograms show a deviation toward positive differences to the moist pseudoadiabat and toward negative differences with the dry adiabat suggesting that the global average of precipitating clouds are conditionally stable but close to a saturated pseudoadiabat like those on Figures 2 and 3. Clear scenes are found to be slightly unstable to dry convection but close to the dry adiabat in the midtroposphere, while precipitating scenes are still conditionally stable but very close to a saturated pseudoadiabat. This statistical result coincides with the observation made for the specific cases shown in Figures 3 and 2, which suggests that they are representative of the physical thermodynamic processes occurring globally.

Figure 5 uses refractivity,  $N$ , as a surrogate for altitude. Using the strong dependence of  $N$  on water vapor mixing ratio, this vertical coordinate compares better states with comparable temperature and atmospheric water vapor combinations that may occur at different heights. To connect the analysis in these figures with how the thermodynamics change as a function of height, Figure 6 shows the differences in averages from the 2-D histograms in the previous figure when they compare the dry adiabat and saturated pseudoadiabat with the RO gradients as a function of altitude now. Both, the nonprecipitating, red, and the precipitating, black, lines are within one standard deviation of each other. However, some structures are visible in the averaged differences. It is found that the clear scenes (red lines), as determined by a CloudSat reflectivity below  $-20$  dBZ, lie between 20% and 30% of the difference between the saturated and the dry adiabat. At midtropospheric cloud altitudes, both clear and precipitating scenes, based on a TRMM reflectivity above 30 dBZ, have an average refractivity gradient clearly lower than the dry refractivity lapse rate. This is associated with being unstable to dry convection. Clear scenes are slightly closer to the dry adiabat than precipitating scenes in the mid troposphere. Precipitating scenes, however, have refractivity gradients closer to the moist saturated pseudoadiabat that become even absolutely unstable to saturated convection especially in the lower latitudes. In

the lower troposphere, below  $\sim 2$  km, the boundary layer refractivity gradient is sharper in nonprecipitating scenes. This sharpness is often caused by thermal inversions suggesting that precipitating scenes are associated statistically with lower vertical refractivity gradients and smaller boundary layer inversions. At the same time sharp refractivity gradients can cause the RO signal to be lost or have a significant refractivity bias. Additionally,  $N$  from Figure 5 reaches values above 300 refractivity units more often in precipitating than in clear scenes. This can be an effect of both, either clear scenes having less water vapor, or RO losing track more often below 2 km. Because the loss of track is the phenomenon observed in the sharper drop in number of counts in Figure 1, it is consistent with being the loss of track associated to sharp gradients in clear scenes. The smaller contribution from sharp gradients to the precipitating scenes is a sign of more frequent smooth transitions from the midtroposphere into the boundary layer than in clear scenes. Other than noting this increased frequency, the refractivity biases below 2 km cannot be taken for quantitative thermodynamic analysis with much confidence.

#### 4. Summary and Conclusions

GNSS RO sounding of the atmosphere can constrain directly the average large-scale thermodynamics inside clouds because it escapes the limitations of other instruments that cannot penetrate clouds, or the radar instruments that can penetrate clouds to measure precipitation but provide no thermodynamical information. Radiometeorological considerations are used as a diagnostic tool that finds a transition in the thermodynamics driving the lapse rate and in stability to convection at the top of precipitating layers. RO high vertical resolution adds fine-scale vertical information to analyses otherwise having to rely on total column values such as those connecting total precipitable water vapor to the occurrence of rain (e.g., Schiro et al., 2016). The vertical information in RO additionally detects the vertical changes in stability to convection and discriminates what atmospheric layers control rain. RO profiles can thus improve our understanding of global processes internal to precipitating clouds when they are collocated with precipitation information, as done here with TRMM, or in the future with Polarimetric RO (Cardellach et al., 2015; Padullés et al., 2016) as planned with the PAZ satellite, or with cloud information as given by CloudSat.

RO profiles at the tropics suggest that lapse rates approach the Clausius-Clapeyron equation globally on a planetary scale with an overall constant, nearly saturated, relative humidity and its associated temperature lapse rate of 6 K/km (e.g., Bezold, 1888; Dutton, 1976). RO profiles also measure the departure from stability to convection in these observations that is proportional to buoyancy and can be used to validate the ability of models to capture lapse rates and the stability to convection itself, which can help determine the model vertical velocity. Both are proposed to be at the root of discrepancies on how models project the response of heavy precipitation to climate variability (e.g., O'Gorman & Schneider, 2009). GNSS RO observations over extratropical latitudes show that Conditional Instability is frequently observed in precipitation, which is consistent with reports from weather analyses whereby Conditional Symmetric Instability relates 20% of the time to heavy precipitation in cyclones over the North Atlantic Storm track (e.g., Ginton et al., 2017).

The study here finds in Figure 3 and statistically in Figure 6 where does the ECMWF-ERA Interim reanalysis misses changes in conditional instability accompanying precipitation. A challenge in our analysis stemmed from the fact that for a given refractivity at  $z_0$  there are different pairs of pressure and temperature that can propagate down to cross at a single value of constant refractivity with two temperature values (not shown). Each crossing however has a different vertical refractivity gradient. This has been considered in the statistical comparison on Figures 5 and 6, where the 2-D histogram of the differences between vertical refractivity gradients observed and the mean value of all family of propagated dry adiabats and pseudoadiabats for a given refractivity is shown. Low midlatitudes from  $25^\circ$  to  $40^\circ$  show a more uniform agreement with the pseudoadiabat at most heights. Equatorward of  $25^\circ$  latitude this comparison shows an anomaly at the higher altitudes reflected by  $N \sim 100$ . There, precipitating profiles approach more closely a dry adiabat. At lower altitudes, the differences in vertical refractivity gradient show a wavy structure that could be due to the contribution from extensive clouds or multilayered clouds where precipitation is originating only at some heights. This hypothesis deserves further study that requires data beyond the scope of this work. At the lowest altitudes below 2 km, corresponding to the planetary boundary layer, refractivity gradients are smaller in precipitating than in dry scenes, suggesting a smaller thermal or moist gradient than in clear scenes. One potential scenario is that the boundary layer to middle-troposphere transition has more frequent cases of sharp water vapor gradients in the absence of precipitation than in its presence. Only observations that could capture time series of

RO precipitating profiles can help verify if this absence of sharp transitions is either a cause, due to large-scale preconditioning, or a consequence of precipitation.

The approach to infer moist atmospheric thermodynamics and stability against convection within clouds from RO refractivity profiles does not require assumptions based neither on the type of clouds nor the season. The types of conditions that lead to precipitating clouds can vary however depending on season, if it is between continents and oceans, by aerosol abundances, and even over land it is influenced by local surface properties (e.g., Emanuel, 1994; Intergovernmental Panel on Climate Change, 2014; Liu & Zipser, 2005, for more detailed discussions). The method can therefore be applied in more detailed analyses of the different types of clouds and convection that lead to precipitation both over continents and oceans. It can also have technical application for RO retrievals and help improve model-independent  $T$  retrievals like in, for example, de la Torre Juárez & Nilsson, (2003) that try to overcome the uncertainties introduced by using model data in the retrieval of profiles when there is precipitation.

Finally, isothermal and isentropic processes are subsets of the larger class of processes called polytropic, where the energy transfer to the environment is constant and the ratio  $p(z)/\rho^n(z) = \text{constant}$ . For isobaric processes, the polytropic index is  $n = 0$ , isothermal processes have  $n = 1$ , and isentropic processes have  $n = \gamma = C_p/C_v$  in an ideal gas, with  $C_v$  heat capacity at constant volume. Although it is not done here, it is straightforward to apply the previous technique to consider more generic polytropic processes with different indices  $n$ . In this application, finding the polytropic index that best fits the observed changes in refractivity profile gradients would provide a constraint on the amount of energy transfer at each height.

#### Acknowledgments

This work has been carried out at the Jet Propulsion Laboratory/California Institute of Technology under a NASA-ROSES grant from the GEODESY program. Part of RP work was done under the Spanish Fellowship BES-2012-059353 and a final part was supported by an appointment to the NASA Postdoctoral Program at the Jet Propulsion Laboratory, administered by Universities Space Research Association under contract with NASA. EC acknowledges support partly from Spanish Grant ESP2015-70014-C2-2-R and partly from the Radio Occultation Meteorology Satellite Application Facility (ROM SAF) which is a decentralized operational RO processing center under EUMETSAT. COSMIC data were downloaded from <http://cdaac-www.cosmic.ucar.edu>. TRMM data were obtained from <ftp://trmmopen.gsfc.nasa.gov/pub/trmmdat/>, and CloudSat data were found at <http://cloudsat.atmos.colostate.edu/data>. All data servers are gratefully acknowledged.

#### References

- Anthes, R. A., Bernhardt, P. A., Chen, Y., Cucurull, L., Dymond, K. F., Ector, D., et al. (2008). The COSMIC/FORMOSAT-3 mission: Early results. *Bulletin of the American Meteorological Society*, 89, 313–333. <https://doi.org/10.1175/BAMS-89-3-313>
- Baerkgard, K., Buontempo, C., Burrows, C., Culverwell, I., Engeln, A. v., Gliesner, H., et al. (2014). ROPP user guide. II: FM and 1D–Var, version 8. SAF/ROM/METO/UG/ROPP/003, The EUMETSAT Network of Satellite Application Facilities. <http://www.romsaf.org/>
- Bean, B. R., & Dutton, E. J. (1966). *Radiometeorology*. New York: Dover Pub. Inc.
- Bezold, v. W. (1888). Zur thermodynamik der atmosphäre. Pts. I, II, Sitz. K. Preuss. Akad. Wissensch. Berlin, XLVI, 1189–1206; Gesammelte Abhandlugen. <https://ia902308.us.archive.org/4/items/sitzungsberichte1888deutsch/sitzungsberichte1888deutsch.pdf>
- Biondi, R., Ho, S.-P., Randel, W. J., Syndergaard, S., & Neubert, T. (2013). Tropical cyclone cloud-top height and vertical temperature structure detection using GPS radio occultation measurements. *Journal of Geophysical Research: Atmospheres*, 118, 5247–5259. <https://doi.org/10.1002/jgrd.50448>
- Biondi, R., Randel, W. J., Ho, S.-P., Neubert, T., & Syndergaard, S. (2012). Thermal structure of intense convective clouds derived from GPS radio occultations. *Atmospheric Chemistry and Physics*, 12, 5309–5318. <https://doi.org/10.5194/acp-12-5309-2012>
- Bonafoni, S., & Biondi, R. (2016). The usefulness of the Global Navigation Satellite Systems (GNSS) in the analysis of precipitation events. *Atmospheric Research*, 167, 15–23. <https://doi.org/10.1016/j.atmosres.2015.07.011>
- Bretherton, C. S., Peters, M. E., & Back, L. E. (2004). Relationships between water vapor path and precipitation over the tropical oceans. *Journal of Climate*, 17, 1517–1528. [https://doi.org/10.1175/1520-0442\(2004\)0171517:RBWVPA2.0.CO;2](https://doi.org/10.1175/1520-0442(2004)0171517:RBWVPA2.0.CO;2)
- Cardellach, E., Padullés, R., Tomas, S., Turk, F. J., Ao, C. O., & de la Torre-Juárez, M. (2017). Probability of intense precipitation from polarimetric GNSS radio occultation observations. *Quarterly Journal of the Royal Meteorological Society*, 53, 1. <https://doi.org/10.1002/qj.3161>
- Cardellach, E., Tomas, S., Oliveras, S., Padullés, R., Rius, A., de la Torre-Juárez, M., et al. (2015). Sensitivity of PAZ LEO polarimetric gnss radio-occultation experiment to precipitation events. *IEEE Transactions on Geoscience and Remote Sensing*, 53(1), 190–206. <https://doi.org/10.1109/TGRS.2014.2320309>
- de la Torre Juárez, M., & Nilsson, M. (2003). On the detection of water vapor profiles and thin moisture layers from atmospheric radio occultations. *Journal of Geophysical Research*, 108(D9), 4276. <https://doi.org/10.1029/2002JD002880>
- Dutton, J. A. (1976). *The ceaseless wind: An introduction to the theory of atmospheric motion*, pp. 640. Mineola: Dover Publications.
- Emanuel, K. A. (1994). *Atmospheric convection*, pp. 580. New York: Oxford University Press.
- Emanuel, K. A., Neelin, D. J., & Bretherton, C. S. (1994). On large-scale circulations in convecting atmospheres. *Quarterly Journal of the Royal Meteorological Society*, 120, 1111–1143. <https://doi.org/10.1002/qj.49712051902>
- Glinton, M. R., Gray, S. L., Chagnon, J. M., & Morcrette, C. J. (2017). Modulation of precipitation by conditional symmetric instability release. *Atmospheric Research*, 185, 186–201. <https://doi.org/10.1016/j.atmosres.2016.10.013>
- Hertz, H. (1884). Graphische methode zur bestimmung der adiabatischen zustandsänderungen feuchter luft. *Meteor Ztschr*, 1, 421–431.
- Hocke, K. (1997). Inversion of GPS meteorology data. *Annales Geophysicae*, 15, 443–450. <https://doi.org/10.1007/s00585-997-0443-1>
- Intergovernmental Panel on Climate Change (2014). Climate change 2013—The physical science basis: Working group I contribution to the fifth assessment report of the intergovernmental panel on climate change. <https://www.cambridge.org/core/books/climate-change-2013-the-physical-science-basis/BE9453E500DEF3640B383BADD332C3E>
- Kotlarski, S., Keuler, K., Christensen, O. B., Colette, A., Deque, M., Gobiet, A., et al. (2014). Regional climate modeling on European scales: A joint standard evaluation of the EURO-CORDEX RCM ensemble. *Geoscientific Model Development*, 7, 1297–1333. <https://doi.org/10.5194/gmd-7-1297-2014>
- Kummerow, C., Barnes, W., Kozu, T., Shiue, J., & Simpson, J. (1998). The tropical rainfall measuring mission (TRMM) sensor package. *Journal of Atmospheric and Oceanic Technology*, 15, 809–816. [https://doi.org/10.1175/1520-0426\(1998\)015<0809:TTRMMT>2.0.CO;2](https://doi.org/10.1175/1520-0426(1998)015<0809:TTRMMT>2.0.CO;2)
- Kursinski, E. R., Hajj, G. A., Leroy, S. S., & Herman, B. (2000). The GPS radio occultation technique. *Terrestrial, Atmospheric and Oceanic Sciences*, 11(1), 53–114. <https://doi.org/10.3319/TAO.2000.11.1.53>
- Kursinski, E. R., Hajj, G. A., Schofield, J. T., Linfield, R. P., & Hardy, K. R. (1997). Observing earth's atmosphere with radio occultation measurements using the global positioning system. *Journal of Geophysical Research*, 102(D19), 23429–23465. <https://doi.org/10.1029/97JD01569>



- Liu, C., & Zipser, E. J. (2005). Global distribution of convection penetrating the tropical tropopause. *Journal of Geophysical Research*, 110, D23104. <https://doi.org/10.1029/2005JD006063>
- Lukes, G. D. (1944). Radio-meteorological forecasting by means of the thermodynamics of the modified refractive index, *Third Conference on Propagation*. Washington D.C.: Committee on Propagation, NDRC, pp. 107–113. Nov 16-17.
- Mauritsen, T., & Stevens, B. (2015). Missing iris effect as a possible cause of muted hydrological change and high climate sensitivity in models. *Nature Geoscience*, 8, 346–351. <https://doi.org/10.1038/ngeo2414>
- O’Gorman, P. A., & Schneider, T. (2009). The physical basis for increases in precipitation extremes in simulations of 21st-century climate change. *Proceedings of the National Academy of Sciences of the United States of America*, 106, 14,773–14,777. <https://doi.org/10.1073/pnas.0907610106>
- Padullés, R., Cardellach, E., de la Torre Juárez, M., Tomás, S., Turk, F. J., Oliveras, S., et al. (2016). Atmospheric polarimetric effects on GNSS radio occultations: The ROHP-PAZ field campaign. *Atmospheric Chemistry and Physics*, 16, 635–649. <https://doi.org/10.5194/acp-16-635-2016>
- Padullés, R., Cardellach, E., Wang, K.-N., Ao, C. O., Turk, F. J., & de la Torre Juárez, M. (2018). Assessment of GNSS radio occultation refractivity under heavy precipitation. *Atmospheric Chemistry and Physics*, 18, 11,697–11,708. <https://doi.org/10.5194/acp-18-11697-2018>
- Peng, G. S., de la Torre-Juarez, M., Farley, R. W., & Wessel, J. E. (2006). Impacts of upper tropospheric clouds on GPS radio refractivity. *2006 IEEE Aerospace Conference*, 6, 1–6. <https://doi.org/10.1109/AERO.2006.1655899>
- Phillips, T. J., Potter, G. L., Williamson, D. L., Cederwall, R. T., Boyle, J. S., Fiorino, M., et al. (2004). Evaluating parameterizations in general circulation models: Climate simulation meets weather prediction. *Bulletin of the American Meteorological Society*, 85, 1903–1915. <https://doi.org/10.1175/BAMS-85-12-1903>
- Platnick, S., King, M. D., Ackerman, S. A., Menzel, W. P., Baum, B. A., Riedl, C., & Frey, R. A. (2003). The MODIS cloud products: Algorithms and examples from terra. *IEEE Transactions on Geoscience and Remote Sensing. Aqua Special Issue*, 41, 459–473. <https://doi.org/10.1109/TGRS.2002.808301>
- Rodwell, M. J., & Palmer, T. N. (2007). Using numerical weather prediction to assess climate models. *Quarterly Journal of the Royal Meteorological Society*, 133, 129–146. <https://doi.org/10.1002/qj.23>
- Schiro, K. A., Neelin, J. D., Adams, D. K., & Lintner, B. R. (2016). Deep convection and column water vapor over tropical land vs. tropical ocean: A comparison between the amazon and the tropical western pacific. *Journal of the Atmospheric Sciences*, 73. <https://doi.org/10.1175/JAS-D-16-0119.1>
- Solheim, F. S., Vivkanandan, J., Ware, R. H., & Rocken, C. (1999). Propagation delays induced in GPS signals by dry air, water vapor, hydrometeors, and other particulates. *Journal of Geophysical Research*, 104, 9663–9670. <https://doi.org/10.1029/1999JD900095>
- Stephens, G. L., Vane, D. G., Boain, R. J., Mace, G. G., Sassen, K., Wang, Z., et al. (2002). The cloudSat mission and the A-train: A new dimension of space-based observations of clouds and precipitation. *Bulletin of the American Meteorological Society*, 83(12), 1771–1790. <https://doi.org/10.1175/BAMS-83-12-1771>
- Thayer, D. (1974). An improved equation for the radio refractive index of air. *Radio Science*, 9, 803–807. <https://doi.org/10.1029/RS009i010p00803>
- Vautard, R., Gobiet, A., Jacob, D., Belda, M., Colette, A., Deque, M., et al. (2013). The simulation of european heat waves from an ensemble of regional climate models within the euro-cordex project. *Climate Dynamics*, 41, 2555–2575. <https://doi.org/10.1007/s00382-013-1714-z>
- Vergados, P., Luo, Z. J., Emanuel, K., & Mannucci, A. J. (2014). Observational tests of hurricane intensity estimations using GPS radio occultations. *Journal of Geophysical Research: Atmospheres*, 119, 4. <https://doi.org/10.1002/2013JD020934>
- Wang, K.-N., de la Torre Juárez, M., Ao, C. O., & Xie, F. (2017). Correcting negatively biased refractivity below ducts in GNSS radio occultation: An optimal estimation approach towards improving planetary boundary layer (PBL) characterization. *Atmospheric Measurement Techniques*, 10(12), 4761–4776. <https://doi.org/10.5194/amt-10-4761-2017>
- Wulfmeyer, V., Hardesty, R. M., Turner, D. D., Behrendt, A., Cadeddu, M. P., di Girolamo, P., et al. (2015). A review of the remote sensing of lower tropospheric thermodynamic profiles and its indispensable role for the understanding and the simulation of water and energy cycles. *Reviews of Geophysics*, 53, 819–895. <https://doi.org/10.1002/2014RG000476>
- Xian, T., & Fu, Y. (2015). Characteristics of tropopause-penetrating convection determined by TRMM and COSMIC GPS radio occultation measurements. *Journal of Geophysical Research: Atmospheres*, 120, 7006–7024. <https://doi.org/10.1002/2014JD022633>
- Yang, S., & Zou, X. (2017). Dependence of positive refractivity bias of GPS RO cloudy profiles on cloud fraction along GPS RO limb tracks. *GPS Solutions*, 21, 499–509. <https://doi.org/10.1007/s10291-016-0541-1>
- Yang, S., & Zou, X. (2017). Lapse rate characteristics in ice clouds inferred from GPS RO and CloudSat observations. *Atmospheric Research*, 197, 105–112. <https://doi.org/10.1016/j.atmosres.2017.06.024>